Visualizing Anisotropic Oxygen Diffusion in Ceria under Activated Conditions

Liang Zhu,[1,2] Xin Jin,[1,2] Yu-Yang Zhang,[2,*] Shixuan Du,[1,2,5] Lei Liu,[3,†] Tijana Rajh,[4] Zhi Xu,[1,2,5]
Wenlong Wang,[1,2,5] Xuedong Bai,[1,2,5,‡] Jianguo Wen,[4,§] and Lifen Wang[1,4,‖]

[1]*Beijing National Laboratory for Condensed Matter Physics, Institute of Physics, Chinese Academy of Sciences, Beijing 100190, China*
[2]*School of Physical Sciences and CAS Center for Excellence in Topological Quantum Computation,*
University of Chinese Academy of Sciences, Beijing 100190, China
[3]*Department of Materials Science and Engineering, College of Engineering, Peking University, Beijing 100871, China*
[4]*Center for Nanoscale Materials, Argonne National Laboratory, Lemont, Illinois 60439, USA*
[5]*Songshan Lake Materials Laboratory, Dongguan, Guangdong 523808, China*

(Received 25 October 2019; revised manuscript received 16 December 2019; accepted 8 January 2020; published 5 February 2020)

Oxygen reactivity plays a key role in the performance of ceria-based catalysts. Aberration-corrected transmission electron microscopy and molecular dynamics simulations were used to study the oxygen atom diffusion in ceria under activated conditions. Reactive oxygen atom and its real-time diffusion were visualized. The interplay between cerium and oxygen atoms originating from a Coulomb interaction was revealed by the out-of-plane buckling of cerium atoms associated with oxygen transport. Anisotropic oxygen atom diffusion that depends on crystal orientations was discovered, demonstrating a preferential [001] crystallographic diffusion pathway. These findings reveal prospects for applications of anisotropic orientation-relevant fluorite-structured oxides.

DOI: 10.1103/PhysRevLett.124.056002

Cerium oxide (CeO_2), also known as ceria, is a typical oxide catalyst [1–3] that has been extensively investigated in the photocatalytic water splitting for hydrogen production [4] and solid-oxide fuel cells for energy storage [5]. Recyclable release and storage of oxygen atoms is the key process for all of these applications [6]. The formation of oxygen vacancies and the migration of oxygen atoms under external stimuli serve as the basis for functional oxide materials and related devices [7]. Real-time visualization of active oxygen vacancies and the exploration of oxygen diffusion pathways on the atomic scale will give rise to the deep understanding of the structure-property relationships, eventually facilitating the control of catalytic processes [8–10].

The structural characterization using transmission electron microscopy (TEM) reveals the key phenomena for ceria redox process, for example, varied surface reconstructions upon the Ce reduction from Ce^{4+} to Ce^{3+} [11,12]. However, real-time visualization of dynamic oxygen atoms with spatial and, in particular, elementary resolution was a challenge due to aberration of the objective lens. Previously reported negative spherical aberration-corrected TEM suggests that atomic resolution in oxides is promising, as demonstrated in $SrTiO_3$ [13]. For functional oxides under activated conditions, advanced methods with the enhanced contrast of oxygen atoms are required for the atom motion tracking and quantitative measurements. Here, taking ceria, the fluorite-structured catalyst, as a model system, we demonstrate that dynamic oxygen diffusion and its anisotropic character can be directly visualized using the aberration-corrected TEM. The real-time interplay between the cerium cationic lattice rearrangement and the anisotropic diffusion of oxygen atoms is unveiled at the sub-angstrom resolution. The combined study by high-resolution TEM characterizations, density functional theory calculations, and molecular dynamics simulations presents a powerful tool for understanding the reactive nature of oxygen atoms in catalysts at the atomic scale.

CeO_2 under the ambient condition has a fluorite structure. We apply the aberration-corrected TEM to determine the structure of CeO_2 nanoparticles in the ultrahigh vacuum system. The details are provided in Fig. 1 in the Supplemental Material [14]. Under the illumination of the 200 kV accelerated electron, pristine fluorite-structured CeO_2 transits to Ce_2O_3 with a bixbyite structure (space group: Ia3) [35,36]. The atomic schematic of fluorite CeO_2 and bixbyite Ce_2O_3 is shown in Fig. 1(a). Especially, in the bixbyite structure Ce atoms split into *d*-site and *b*-site types according to the different coordination with O atoms and vacancies. All atoms slightly deviate from sites in the cubic unit of the fluorite structure. Figure 1(b) shows the overview TEM image of a ceria nanoparticle. With a typical imaging beam flux on the order of $10^4\ e^-/\text{Å}^2$ s, the 200 kV accelerated incident electrons transfer energy up to 33 eV to O atoms in CeO_2, which is beyond the previous estimate of the threshold displacement energy (about 27 eV) [37], enabling the observation of the fluorite-bixbyite structure transition via the radiolysis effect. By adjusting the beam flux, release and acquisition of oxygen atoms in

0031-9007/20/124(5)/056002(6)

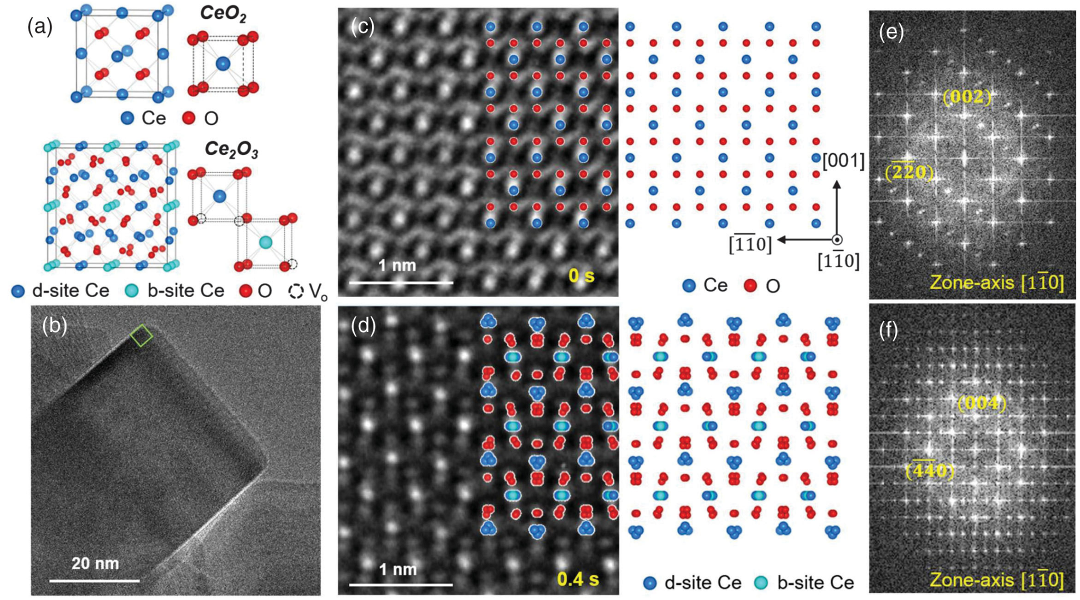

FIG. 1. Atomic resolution TEM imaging of the structural evolution in ceria. (a) Atomic configurations of CeO_2 (top half) and Ce_2O_3 (bottom half). (b) Low-magnification TEM image of the CeO_2 nanoparticle. (c),(d) Snapshot TEM images of the near-edge area in the nanoparticle viewed along the $[1\bar{1}0]$ crystallographic direction superposing with relaxed atomic configurations of CeO_2 and Ce_2O_3. Bright and gray spots in TEM images correspond to Ce and O atom columns, respectively. (e),(f) Diffractogram for (c) and (d).

nanoparticles can be initiated repeatedly. Figures 1(c) and 1(d) show snapshot TEM images of the near-edge area of the nanoparticle during the radiolysis. We took the view along the $\langle 110 \rangle$ crystallographic direction so that Ce and O atom columns are well separated and can thus be easily distinguished for both fluorite ceria and bixbyite ceria. Atomic models of fluorite CeO_2 and bixbyite Ce_2O_3 are superposed on the TEM images, highlighting both Ce and O atomic positions. Corresponding diffractograms of the TEM images as shown in Figs. 1(e) and 1(f) further verify the structures.

To trace the diffusion path of O atoms in ceria, sequential TEM images with a time interval of 0.2 s were recorded [Figs. 2(a)–2(d)] to capture intermediate states during reduction (fluorite CeO_2 to bixbyite Ce_2O_3). The interplay between cerium and oxygen atoms has been revealed.

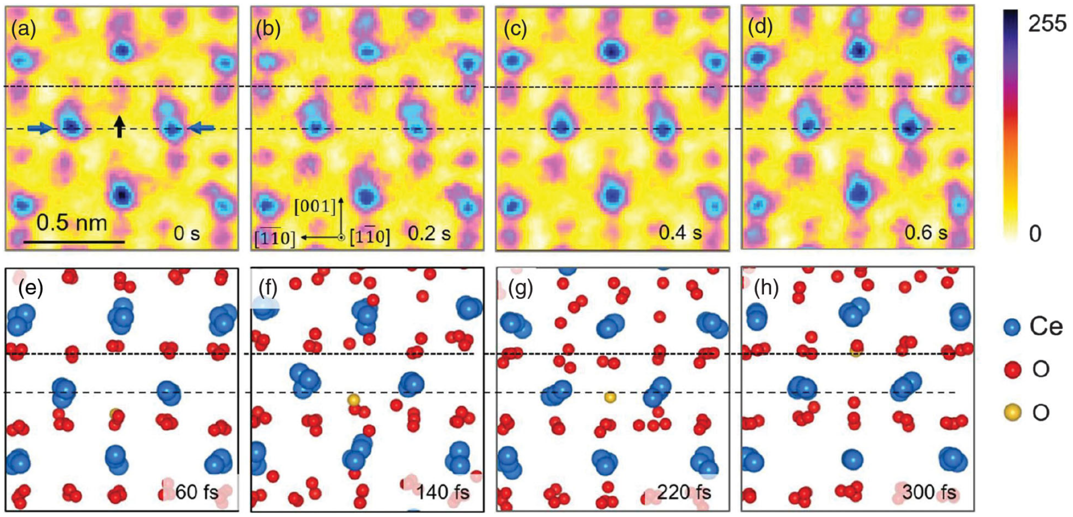

FIG. 2. The interplay between Ce atom arrangement and oxygen vacancy diffusion. (a)–(d) Sequential TEM images showing rearrangement of Ce and O layers along the [001] crystallographic direction. TEM images are colored for clarity and their contrast is inverted. Blue spots with a high density represent Ce column positions. Pink spots with a low intensity show O column positions. $t = 0$ s is the starting time for the real-time recording. (e)–(h) Snapshots of *ab initio* molecular dynamics simulation. Blue and red atoms represent Ce and O atoms, respectively. Yellow atoms are diffusing O atoms.

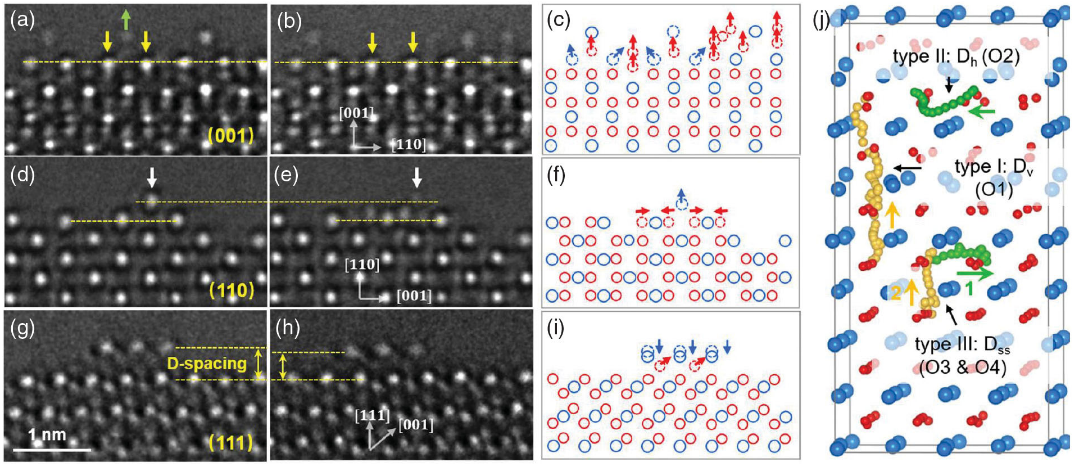

FIG. 3. Low-index surface dynamics in ceria under reduction. (a),(b) TEM image snapshots of the (100) surface. (c) Atomic configuration derived from video data. Blue and red circles represent Ce columns and O positions, respectively. (d),(e) Serial TEM images of the (110) surface flattening under reduction. (f) Atomic configuration derived from (d)–(e). (g),(h) TEM images of the (111) surface linear defect formation. (i) Atomic configuration derived from (g)–(h). (j) *Ab initio* molecular dynamics simulation calculated trajectory of diffusing O atoms (O1–O4) with three types of diffusion processes.

When focusing on the O atom column (black arrow), the out-of-plane buckling of O atoms along the [001] direction evolves during the reduction. Displacement of the spot for the oxygen column is up to ~40 pm. The local intensity of the spot increases as shown in the sequential TEM images [Figs. 2(a)–2(d)], also see Fig. 2 in the Supplemental Material [14] for more details), indicating the evolution of the O atom concentration in this column. Moreover, the nearest neighboring Ce atom columns (two blue arrows) show the simultaneous out-of-plane buckling clearly. Note that the distance between oxygen and its nearest cerium atom in fluorite-CeO_2 is measured to be ~2.4 Å. When a diffusing O atom travels across the Ce plane, the distance between Ce and O atoms decreases to ~1.9 Å. Thus, the electrostatic force on the Ce atoms gets enhanced dramatically because of the charge redistribution, causing the out-of-plane buckling of Ce atoms and the volume expansion of the CeO_2 cell (see video and Fig. 3 in the Supplemental Material [14] for more details). While electron reduction is the driving force for the O atom migration, the accompanying lattice perturbation of surrounding Ce atoms provides additional resistance, hindering the diffusion of O atoms [38]. More importantly, when considering the lattice symmetry, the optimized oxygen diffusion path with the lowest diffusion barrier may exist while the accompanying perturbation response of the Ce sublattice would be minimized, leading to an anisotropic diffusion of O atoms in ceria.

To get a better understanding of the oxygen diffusion process in CeO_2 during the reduction process, we performed *ab initio* molecular dynamics (MD) simulations. A model structure with half CeO_2 and half Ce_2O_3 was first constructed to simulate the interface of the CeO_2 reduction process (see Fig. 4 in the Supplemental Material [14] for the structure employed in MD simulation). This model is more energetically favorable than structures with a random O vacancy distribution. An MD simulation at 2000 K was carried out and the resulting snapshots are shown in Figs. 2(e)–2(h). The diffusion of O atoms along the [001] direction was observed (illustrated by the motion of the yellow ball). During the O atom diffusion process, the related Ce plane splits in the oxygen-diffusion direction [Figs. 2(f) and 2(g)] and becomes flat again at the end of the process [sparse dashed line in MD snapshots, Figs. 2(e)–2(h)]. MD calculations are in nice agreement

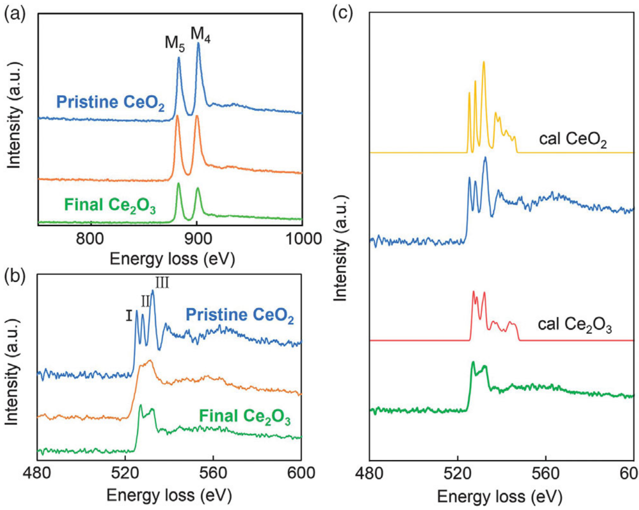

FIG. 4. Intermediate chemical bonding states revealed by electron spectroscopy. (a) Ce *M*-edge evolution during CeO_2 reduction process. (b) O *K*-edge evolution during CeO_2 reduction process. (c) Simulated EELS spectra compared with experimental data. Yellow and red curves are calculated O *K*-edge EELS spectra for CeO_2 and Ce_2O_3, respectively.

with the experimental findings, further revealing the interplay between O atom diffusion and out-of-plane buckling of Ce lattices.

We then further studied the dynamic behavior of the (001), (110), and (111) surfaces during the reduction to evaluate the diffusion path of O atoms. Figure 3 displays comparisons of the atomic configurations of the three exposed low-index surfaces with distinct deformation features during the structural transition. For the (001) surface, frequent events of atom diffusion into the vacuum (more than 20 recorded) were recognized, demonstrating that the (001) ceria surface has a very high activity (see video in the Supplemental Material [14]). Figures 3(a) and 3(b) show representative sequential images of the (001) surface during the reduction. The surface was flat and was mostly defined by Ce atom column layers. The two yellow arrows indicate the position of two Ce spots, while the outmost O atoms are highlighted by the green arrow. With the ongoing of the reduction process, the marked O atoms escaped from the crystal. Simultaneously, the distance between the two adjacent Ce atoms increased by ~10% which is ascribed to the local enhanced Coulomb interaction [8,39]. The dynamics of O atom diffusion and local Ce atom response is illustrated by the schematic in Fig. 3(c). In addition, although the O atom diffusion path in the bulk CeO_2 is hard to be identified, the observed continuous O atom-releasing events along the [001] direction at (001) surface not only prove the high activity of the (001) plane, but also indicate the preferential diffusion path of O atoms. As discussed previously, such anisotropic diffusion phenomena could be attributed to the varying local lattice perturbation corresponding to the charge redistribution. Contrary to the (001) facet, (110) surface shows much lower O atom diffusion activity [40]. O atoms escaping into the vacuum were barely observed, while migration along the [001] direction on the surface was easily established, as shown in Figs. 3(d)–3(f). In sharp contrast to the (001) and (110) surfaces, after the examination of tens of nanoparticles no apparent atom migration or surface reconstruction were observed on the O-terminated (111) surface, demonstrating the highly robust atomic configuration. On Ce-terminated (111) surfaces [41–43], instead of the independent diffusion of single atoms, collective behavior involving planar O atoms has been recorded [Figs. 3(g)–3(h)]. Figure 3(g) shows a small bump of Ce atoms that was occasionally found on the (111) surface keeping a certain plane distance (D spacing) for storing O atoms. During the reduction process, the D spacing decreases with the escaping of one oxygen atomic layer. The most probable scenario for the collective release of oxygen atoms on the Ce-terminated (111) surface is the surface reconstruction induced by the polar nature and instability [44].

We further analyzed the MD results, and three types of oxygen atom diffusion processes were identified (see Fig. 5 in the Supplemental Material [14] for details). The motion trajectory of one O atom is highlighted in Fig. 3(j). The first type is denoted by D_v, in which O atoms start from the CeO_2 part and diffuse along the [001] direction. In the second diffusion process, O atoms diffuse into the coplanar neighboring vacancy site, which is denoted by D_h. Here, O atoms will not diffuse from the CeO_2 regime to the Ce_2O_3 regime, thus contributing little to the reduction of CeO_2. The third type is the step-by-step diffusion, denoted by D_{ss}. D_{ss} consists of two sequential processes. First, an O atom (represented by O3) diffuses into a coplanar neighboring vacancy site, which creates a vacancy at its original location. Then, an O atom located in the next layer (represented by O4) diffuses along the [001] direction and fills the vacancy created by the O3 diffusion. Furthermore, the energy barrier for O atom diffusion was calculated (see Fig. 6 in Supplemental Material [14]). An O atom will overcome a barrier of 0.74 eV in D_v, which is comparable to previously reported experimental results [45]. O atoms diffuse in the equivalent $\langle 001 \rangle$ direction in all three types of diffusion paths. Therefore, the three types of diffusion paths revealed by the simulation are consistent with our experimental findings that O prefers to diffuse in the $\langle 001 \rangle$ direction.

The electron energy loss spectroscopy (EELS) measurement of the Ce and O spectra, which reflects the average valency properties and chemical bonding, are also recorded during the structural phase transition (Fig. 4). The Ce spectra feature two sharp and strong peaks located at 883 and 901 eV, corresponding to the M_5 and M_4 edges, respectively. The two peaks originate from the transition of electrons from the spin-orbit split levels $3d_{5/2}$ and $3d_{3/2}$ to the unoccupied $4f$ states [46]. The M_4/M_5 intensity ratio decreases from 1.12 to 0.75, with an increase in concentration of trivalent Ce depending on the valence state of Ce, which is in agreement with previously reported values [36].

The evolution of the O K edge is shown in Fig. 4(b). Pristine oxygen K edge for CeO_2 has three main peaks marked by `I`, `II`, and `III`. The spectrum for Ce_2O_3 shows two of these characteristic peaks with a slight peak shift and variation in relative intensities [15]. Peak `I` originates from the O-1s electron transition to the p-like component of the hybrid Ce $4f$ and O $2p$ states, suggesting an unoccupied $4f$ state which is characteristic of tetravalent Ce. Peaks `II` and `III` arise because of the hybridization of unoccupied O $2p$-like states with the crystal-field split Ce $5d$-e_g and Ce $5d$-t_{2g} states, representing a strong local atomic arrangement influence of CeO_8 or CeO_6 [47]. After the structure transition, all three peaks become broader, while the contribution of peak `II` increases significantly with reduction, leading to a different shape that is supported by the simulations result as shown in Fig. 4(c). The highly dynamic diffusion of O atoms not only gives rise to the accompanying local Ce lattice distortion, but also the nonsaturated chemical bonding due to transient nonstoichiometric configurations.

In summary, visualization of O atoms and real-time motion tracking by the aberration-corrected TEM demonstrated the preferred ⟨001⟩ diffusion path in ceria, which was verified by DFT calculation and MD simulations. The attendant effects from O atom diffusion, including the neighboring Ce out-of-plane buckling and the variation of the chemical bonding, were demonstrated, describing barriers for the O atom diffusion. The perturbation response of Ce lattice has an anisotropic character, suggesting a micromechanism for the anisotropic oxygen diffusion activities. When considering that the interaction between cation ions and oxygen atoms is similar in fluorite-structure oxides, here the newly established mechanism for the oxygen diffusion in ceria further implies that the accompanying response of local cation atoms may be universal, leading to the same anisotropic oxygen diffusion behaviors in other functional fluorite-structure oxides.

This work was supported by the National Natural Science Foundation (11974388, 11974001, 51872284, U1932153, 21872172, 21773303, and 51421002), the National Key R&D Program (2016YFA0300804, 2016YFA0300903, 2018YFA0305800, 2019YFA0307801, and 2019YFA0308500), the Program from Chinese Academy of Sciences (ZDYZ2015-1, Y8K5261B11, XDB30000000, XDB28000000, and XDB07030100), and Beijing Natural Science Foundation (2192022, Z190011). L. W. is grateful for the support from the Youth Innovation Promotion Association of CAS (2020009). This work, including Argonne Chromatic Aberration-corrected TEM, was performed at the Center for Nanoscale Materials, an Office of Science user facility, supported by the U.S. Department of Energy, Office of Science under Contract No. DE-AC02-06CH11357.

L. Z. and X. J. contributed equally to this work.

---

[*] zhangyuyang@ucas.ac.cn
[†] leiliu1@pku.edu.cn
[‡] xdbai@iphy.ac.cn
[§] jwen@anl.gov
[‖] wanglf@iphy.ac.cn

[1] L. Nie, D. Mei, H. Xiong, B. Peng, Z. Ren, X. I. P. Hernandez, A. Delariva, M. Wang, M. H. Engelhard, L. Kovarik, A. K. Datye, and Y. Wang, Science **358**, 1419 (2017).

[2] Q. Fu, H. Saltsburg, and M. Flytzani-Stephanopoulos, Science **301**, 935 (2003).

[3] J. A. Farmer and C. T. Campbell, Science **329**, 933 (2010).

[4] R. Farrauto, S. Hwang, L. Shore, W. Ruettinger, J. Lampert, T. Giroux, Y. Liu, and O. Ilinich, Annu. Rev. Mater. Res. **33**, 1 (2003).

[5] E. P. Murray, T. Tsai, and S. A. Barnett, Nature **400**, 649 (1999).

[6] C. T. Campbell and C. H. F. Peden, Science **309**, 713 (2005).

[7] Z.-P. Liu, S. J. Jenkins, and D. A. King, Phys. Rev. Lett. **94**, 196102 (2005).

[8] F. Esch, S. Fabris, L. Zhou, T. Montini, C. Africh, P. Fornasiero, G. Comelli, and R. Rosei, Science **309**, 752 (2005).

[9] N. V. Skorodumova, S. I. Simak, B. I. Lundqvist, I. A. Abrikosov, and B. Johansson, Phys. Rev. Lett. **89**, 166601 (2002).

[10] T. W. Hansen, J. B. Wagner, P. L. Hansen, S. Dahl, H. Topsøe, and C. J. H. Jacobsen, Science **294**, 1508 (2001).

[11] P. A. Crozier and T. W. Hansen, MRS Bull. **40**, 38 (2015).

[12] H. Topsøe, J. Catal. **216**, 155 (2003).

[13] C. L. Jia, M. Lentzen, and K. Urban, Science **299**, 870 (2003).

[14] See Supplemental Material at http://link.aps.org/supplemental/10.1103/PhysRevLett.124.056002 for a discussion of the Materials and Methods, HRTEM image calculation to compare with experimental images, intensity profiles of dynamic O in ceria, evaluation of the column interactions within the atoms in ceria during oxygen diffusion, the structure employed in MD simulation, evolution of the fractional coordinate of four representative O atoms in MD simulation, oxygen diffusion process in partially reduced CeO_2, combinations of O K-edge EELS spectra of the initial and final state for comparison with intermediate state, O atom diffusion in 1000 K *ab initio* MD simulation, and real-time TEM video of ceria nanoparticle under the reduction processes, which includes Refs. [15–34].

[15] M. Nolan, S. C. Parker, and G. W. Watson, Surf. Sci. **595**, 223 (2005).

[16] O. Kraynis, J. Timoshenko, J. Huang, H. Singh, E. Wachtel, A. I. Frenkel, and I. Lubomirsky, Inorg. Chem. **58**, 7527 (2019).

[17] G. Kresse and J. Furthmuller, Comput. Mater. Sci. **6**, 15 (1996).

[18] G. Kresse and J. Hafner, Phys. Rev. B **47**, 558 (1993).

[19] G. Kresse and J. Hafner, Phys. Rev. B **48**, 13115 (1993).

[20] P. E. Blochl, Phys. Rev. B **50**, 17953 (1994).

[21] J. P. Perdew, K. Burke, and M. Ernzerhof, Phys. Rev. Lett. **77**, 3865 (1996).

[22] S. L. Dudarev, G. A. Botton, S. Y. Savrasov, C. J. Humphreys, and A. P. Sutton, Phys. Rev. B **57**, 1505 (1998).

[23] M. Nolan, S. Grigoleit, D. C. Sayle, S. C. Parker, and G. W. Watson, Surf. Sci. **576**, 217 (2005).

[24] D. A. Andersson, S. I. Simak, B. Johansson, I. A. Abrikosov, and N. V. Skorodumova, Phys. Rev. B **75**, 035109 (2007).

[25] N. Daelman, M. Capdevila-Cortada, and N. Lopez, Nat. Mater. **18**, 1215 (2019).

[26] S. Nose, Mol. Phys. **52**, 255 (1984).

[27] S. Nose, J. Chem. Phys. **81**, 511 (1984).

[28] Y. S. Su and S. T. Pantelides, Phys. Rev. Lett. **88**, 165503 (2002).

[29] T. J. Pennycook, M. J. Beck, K. Varga, M. Varela, S. J. Pennycook, and S. T. Pantelides, Phys. Rev. Lett. **104**, 115901 (2010).

[30] G. Henkelman and H. Jonsson, J. Chem. Phys. **113**, 9978 (2000).

[31] G. Henkelman, B. P. Uberuaga, and H. Jonsson, J. Chem. Phys. **113**, 9901 (2000).

[32] R. Buczko, G. Duscher, S. J. Pennycook, and S. T. Pantelides, Phys. Rev. Lett. **85**, 2168 (2000).

[33] W. Luo, M. Varela, J. Tao, S. J. Pennycook, and S. T. Pantelides, Phys. Rev. B **79**, 052405 (2009).

[34] K. Kambe, G. Lehmpfuhl, F. Fujimoto, and Z. Naturforsch, Z. Naturforsch. **29A**, 1034 (1974).

[35] I. Riess, R. Koerner, M. Ricken, and J. Noelting, Solid State Ionics **28–30**, 539 (1988).

[36] M. Romeo, K. Bak, J. El Fallah, F. Le Normand, and L. Hilaire, Surf. Interface Anal. **20**, 508 (1993).

[37] V. Piacente, G. Bardi, L. Malaspina, and A. Desideri, J. Chem. Phys. **59**, 31 (1973).

[38] M. Nolan, J. E. Fearon, and G. W. Watson, Solid State Ionics **177**, 3069 (2006).

[39] H. Y. Li, H. F. Wang, X. Q. Gong, Y. L. Guo, Y. Guo, G. Z. Lu, and P. Hu, Phys. Rev. B **79**, 193401 (2009).

[40] J. Kullgren, K. Hermansson, and C. Castleton, J. Chem. Phys. **137**, 044705 (2012).

[41] Y. Namai, K. Fukui, and Y. Iwasawa, J. Phys. Chem. B **107**, 11666 (2003).

[42] Y. Namai, K. Fukui, and Y. Iwasawa, Catal. Today **85**, 79 (2003).

[43] Y. Lin, Z. Wu, J. Wen, K. R. Poeppelmeier, and L. D. Marks, Nano Lett. **14**, 191 (2014).

[44] C. Yang, X. Yu, S. Heißler, A. Nefedov, S. Colussi, J. Llorca, A. Trovarelli, Y. Wang, and C. Wöll, Angew. Chem., Int. Ed. **56**, 375 (2017).

[45] H. Tuller and A. Nowick, J. Phys. Chem. Solids **38**, 859 (1977).

[46] L. Douillard, M. Gautier, N. Thromat, M. Henriot, M. J. Guittet, J. P. Duraud, and G. Tourillon, Phys. Rev. B **49**, 16171 (1994).

[47] A. V. Soldatov, T. S. Ivanchenko, S. Della Longa, A. Kotani, Y. Iwamoto, and A. Bianconi, Phys. Rev. B **50**, 5074 (1994).